*Article*

# Cyclic Extrusion Compression Process for Achieving Ultrafine-Grained 5052 Aluminum Alloy with Eminent Strength and Wear Resistance

**Jianxin Wu [1], Mahmoud Ebrahimi [2],\*, Shokouh Attarilar [3], Ceren Gode [4] and Mohammad Zadshakoyan [5]**

[1] Collaborative Innovation Center of Steel Technology, University of Science and Technology Beijing, Beijing 100083, China
[2] Department of Mechanical Engineering, Faculty of Engineering, University of Maragheh, Maragheh 83111-55181, Iran
[3] Department of Materials Engineering, Faculty of Engineering, University of Maragheh, Maragheh 83111-55181, Iran
[4] Department of Machinery and Metal Technologies, Technical Sciences and Vocational High School, Pamukkale University, Denizli 20160, Turkey
[5] Department of Manufacturing and Production Engineering, Faculty of Mechanical Engineering, University of Tabriz, Tabriz 51666-16471, Iran
\* Correspondence: ebrahimi@maragheh.ac.ir; Tel.: +98-914-401-7268

**Abstract:** Previous studies have yet to show a consistent effect of severe plastic deformation (SPD) processing on the wear behavior of different metals and alloys. To fill this scientific gap, this study investigated the effect of the cyclic extrusion compression (CEC) process, as one of the prominent SPD techniques, on the wear behavior of AA5052. In addition, the microstructure evolution and mechanical properties of the sample before and after the process were experimentally examined and studied. It was found that the yield and ultimate tensile strength of the AA5052 improved significantly after the first pass, while the elongation-to-failure decreased considerably. Further, the subsequent passes mildly changed the trend of increasing strength and reducing elongation-to-failure. SEM morphology indicated that the ductile mode of the initial annealed alloy changed to a combination of ductile and brittle failure modes, in which the level of the brittle failure mode increased with the addition of passes. TEM observations showed that the grain refinement during the CEC process included the formation of dislocation cell structures, subgrain boundaries, and low-angle grain boundaries, with the subgrain boundaries initially evolving into low-angle grain boundaries and, eventually, due to the imposition of additional plastic strain, into high-angle grain boundaries. Furthermore, the CEC process and its increased number of passes led to a significant improvement in wear resistance due to the enhanced tensile strength achieved through grain refinement. In this regard, the wear mechanism of the initial alloy was a combination of adhesion and delamination, with the plastic deformation bands changing to plowing bands with decreased adhesive wear during the process. Eventually, oxidization was found to be a mechanism contributing to wear under all conditions.

**Keywords:** severe plastic deformation; AA5052; TEM observation; tensile properties; wear behavior

## 1. Introduction

It is widely recognized and reported that microstructural arrays significantly contribute to distinctive material properties [1–5]. Specifically, grain refinement, in accordance with the Hall–Petch relationship, is an efficient approach for enhancing the monotonic and dynamic properties of materials [6–9]. From this point of view, materials can be classified into three categories: micro-, ultrafine-, and nano-grains. In the last three decades, ultrafine-grained (UFG) and nanostructured (NS) materials have attracted much attention from researchers due to their high performance [10–13]. In this regard, the techniques to

obtain these materials are also of great importance, and they are divided into top-down and bottom-up approaches. Previous studies have shown that severe plastic deformation (SPD) is one of the best techniques to obtain UFG structures [14–16]. Some well-known methods include equal channel angular pressing [17], high-pressure torsion [18], constrained groove pressing [19], constrained studded pressing [20], accumulative roll-bonding [21], planar twist extrusion [22], equal channel forward extrusion [23], multi-directional forging [24,25], friction stir processing [26], cyclic extrusion compression [27], surface mechanical attrition treatment [28], planar twist channel angular extrusion [29], and cyclic close die forging [30].

Among the various SPD methods, cyclic extrusion compression (CEC), introduced by Richert et al. in 1979, is one important technique for grain refinement of metals and alloys that can achieve distinguished monotonic and dynamic mechanical properties [31–35]. Figure 1 schematically shows this process. First, the sample is placed in the inlet channel. Then, compression is performed simultaneously with extrusion during plastic deformation between two inlet and outlet channels using a small-diameter connecting channel in the presence of a back pressure punch [36]. Considering that the sample will eventually return to its initial dimensions, this process can be repeated as many times as necessary to reach the desired plastic strains. Furthermore, in this process, there is no need to take the samples out during successive passes, which is a very important advantage because the processing time is shortened [37].
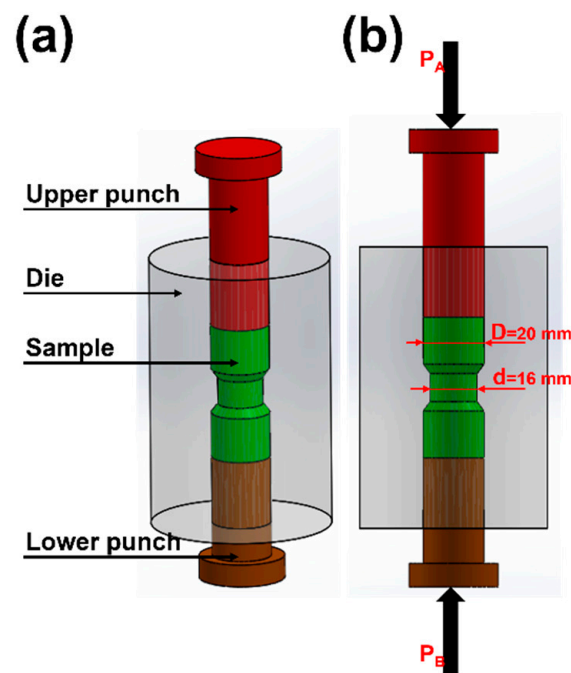


**Figure 1.** Schematic representation of the cyclic extrusion compression (CEC) process: (**a**) the three-dimensional view of the significant die parameters and (**b**) the front view of the CEC process, with an initial diameter and extruded diameters, along with applied pressures.

Magnesium is one of the most influential and widely used alloying elements for aluminum alloys, and it is also the main element in 5000 series alloys (AA5000). Among these allows, 5052 aluminum alloy (AA5052) is an important candidate that is especially utilized in the body panels of cars [38–42]. These non-heat-treatable alloys with moderate strength and resistance to corrosion and wear are readily weldable. Further, Al–Mg alloys can be hardened using cold working processes, such as the mentioned SPD techniques. In this context, automotive, aerospace, architectural, and marine applications are among the most relevant industries.

Several studies have been conducted on the microstructural evolution and mechanical properties of different materials during SPD processing [11,43–47]. However, some of the

secondary properties of processed materials, such as wear, hydrogen absorption, damping, and corrosion behavior, have rarely been studied, even though different behaviors in the processed materials are sometimes detectable from this point of view and various new aspects need to be considered, such as the optimization of SPD methods through modeling and simulation methods [48–53]. Therefore, it is essential to investigate the wear resistance behavior of SPD-processed materials to achieve their optimal use. As is known, the wear of a component leads in practice to an increase in the clearance and loss of precision in moving components; consequently, increasing the wear resistance results in longer service life. Nevertheless, despite the evident significance of wear in industrial applications, there are only a limited number of reports on the wear characteristics of SPD-processed materials, which highlights the necessity of this study.

Furthermore, the effects of SPD processes on the wear behavior of different materials have been reported to be very contradictory. In this regard, favorable effects of SPD processes on tested metals and alloys were reported for several SPD-processed materials: Abd El Aal et al. reported such effects for ECAP-processed Al–Cu alloys [54], Gao et al. for ECAPed-processed Cu–10%Al–4%Fe alloy [55,56], Korshunov et al. for SPD-processed Babbit B83 [57], Wang et al. for SMAT-processed low carbon steel [58], La et al. for ECAP-processed titanium [59], etc. On the other hand, several researchers have reported deteriorations of wear resistance in SPD-processed materials, such as in ECAP-processed Al-12Si alloy by Kucukomeroglu [60] and ARB- and ECAP-processed Al alloys and steel by Kim et al. [61]. In addition, insignificant variations in wear resistance were observed in the studies conducted by Kim et al. on ECAP-processed Al6061 and AZ61 Mg alloys [62], Sato et al. on ECAP-processed Al–Al3Ti alloys [63], and Garbacz et al. on ECAP-processed pure titanium [64]. To address these contradictory findings and consider the industrial importance of the 5000 aluminum alloy series, this study investigated the effect of the CEC process on the wear behavior of AA5052. The reason for choosing the CEC process is due to its potential for industrialization and sample scale-up. Further, AA5052 was selected from other AA5000 alloys due to its wide applications in various automobile, transportation, aircraft, and marine sectors. In addition, the main novelty of this work is that it will help to understand the mechanical properties and wear behavior of AA5052 after the CEC process.

Consequently, AA5052 was processed with the CEC method at room temperature up to failure. Then, the wear behavior, microstructure evolution, and mechanical properties of the alloy before and after the process with different numbers of passes were examined experimentally and investigated systematically.

## 2. Materials and Methods

Commercial 5052 aluminum alloy (AA5052) in an initial rolled state was chosen for this study because of its diverse applications in various industries. The relevant chemical compositions obtained by full-spectrum direct-reading inductively coupled plasma atomic emission spectroscopy included 2.43 wt.% Mg, 0.34 wt.% Cr, 0.29 wt.% Si, 0.27 wt.% Fe, 0.10 wt.% Cu, 0.08 wt.% Mn, 0.07 wt.% Zn, and Al as balance. First, the AA5052 was cut into cylindrical-shaped samples with a length and diameter of 110 mm and 20 mm, respectively, in a lathing machine. Afterward, they were annealed at 380 °C for 2 h and cooled slowly at the furnace down to the ambient temperature. This severe plastic deformation was carried out using the CEC method, with up to four passes at room temperature through a hydraulic pressing machine with a constant velocity of 6 mm/min in the presence of molybdenum disulfide ($MoS_2$) as a lubricant in order to minimize the frictional effects. In this study, the CEC die had inlet and outlet channels of 20 mm diameter and a connecting channel with a diameter of 16 mm. Considering that each pass involved the whole process of extruding the sample from a diameter of 20 to 16 mm, followed by compressing it to the initial diameter, according to the theoretical relationship in Equation (1), the imposed plastic strain in each pass was equal to 0.89 [48,65,66]. In this regard, $D$, $d$, and $N$ represent the initial diameter, extruded diameter, and pass numbers, respectively. Then, the tensile

behavior, fracture analysis, microstructural evolution, and wear resistance of the annealed and CEC-processed samples were examined, compared, and investigated.

$$\varepsilon_{eff} = 4N \ln \frac{D}{d} \tag{1}$$

Tensile testing was conducted using an MTS universal testing machine with a closed-loop servo-hydraulic control at room temperature and an initial strain rate of $1.2 \times 10^{-3} \, s^{-1}$. The 50 mm gauge length specimen dimension was in accordance with ASTM B557M. Each sample state was obtained three times and, based on this, the yield strength and elongation-to-failure values revealed a scatter of ±6%. Note that the tensile testing specimens were cut along the longitudinal direction of the CEC-processed AA5052 samples. The fractography analysis was conducted with an SEM device on annealed and CEC-processed samples after tensile testing. Each test was repeated twice in order to ensure replicability.

Transmission electron microscopy (TEM) was used in order to characterize the microstructure evolution of samples after processing with the CEC method for up to four passes. For TEM images, thin foils of 1 mm thickness were fabricated and ground to a thickness of 80–90 μm. They were then thinned through a double-jet electro polisher in a solution of 20% $HClNO_4$ and 80% methyl at the temperature and voltage of −15 °C and 24 V. It should be mentioned that the thin foils were tilted to align the specimens to the low-index zone axis, which was almost parallel to the direction of incident beam, to attain a better image contrast.

Dry sliding wear tests were performed according to ASTM-G133 on the annealed and the CEC-processed samples with different numbers of passes using a linearly reciprocating ball-on-flat method. The plate-formed specimens prepared for this aim, which had the dimensions of 50 mm × 10 mm × 2 mm, were mechanically ground by SiC paper up to 5000. The applied ball material, diameter, and hardness were tungsten carbide (WC), 5 mm, and 78 HRC, respectively. All wear tests were accomplished with constant frequency, constant stroke length, and line speed of 12 Hz, 40 mm, and 0.28 m/s, respectively, at a testing temperature of 25 ± 2 °C and relative humidity of 58 ± 4%. The 1000 s duration of each test resulted in a total sliding distance of 280 m. All wear specimens were washed before and after the test in an ultrasonic acetone bath for about 8 min and then dried in air. Furthermore, the difference in the weight of the wear specimens before and after the test was calculated using a digital balance device with a sensitivity of 0.0001 g in order to measure wear mass loss. Two normal loads of 2 and 20 N were used for this study. In addition, each test state was repeated at least twice in order to avoid any errors. Equation (2) was utilized to calculate wear quantities, in which *V*, *L*, *K*, *F*, *HV*, and k are the worn volume ($mm^3$), total sliding distance (m), Archard's constant (wear coefficient), applied normal load (N), Vickers hardness value, and specific wear rate ($mm^3$/N·m), respectively [19,67]. Eventually, after testing, FE-SEM and energy-dispersive X-ray spectroscopy (EDX) were employed to analyze the morphology of the worn surfaces.

$$\frac{V}{L} = K\left(\frac{F}{HV}\right) = kF \tag{2}$$

## 3. Results and Discussion

### 3.1. Tensile Properties

The engineering tensile stress–strain curves for the initial annealed state and CEC-processed samples with different numbers of passes, as well as the corresponding values for the yield strength (YS), ultimate tensile strength (UTS), and elongation-to-failure (El), are shown in Figure 2 and listed in Table 1. As can be observed, after applying the first pass of the CEC process to AA5052, the strength improved significantly, while the elongation-to-failure dropped considerably. The improvement in the mechanical properties is usually more significant in the first pass of SPD techniques due to the higher dislocation density compared to samples with increased numbers of passes. Generally, the dislocation density

of the severe plastic deformed sample increases in the initial pass and then gradually decreases due to restoration mechanisms [68]. In this regard, approximately 46% and 25% increases in the YS and UTS of AA5052 were detectable after applying for the first pass, while the elongation-to-failure decreased by about 38.6%. Regarding the subsequent passes of the process, it should be noted that the mentioned trend continued with lower intensity. For example, applying four passes led to increases in YS and UTS by about 73% and 19% and a decrease in elongation-to-failure by about 47% compared to the first-pass CEC-processed sample. Similar results have been previously reported for other metals and alloys processed with various SPD methods [22,69–72]. For instance, Yogesha et al. [72] processed Al–Mg alloy by cryo-rolling and cryo-groove rolling and reported increments in the YS and UTS of about 76% and 71% and a reduction in elongation-to-failure by about 33%. The results of another study on pure aluminum showed increments in the YS and UTS up to 235% and 92% after two passes with the planar twist channel angular extrusion (PTCAE) process compared to the annealed sample, while the elongation-to-failure underwent a 23.1% reduction [22].
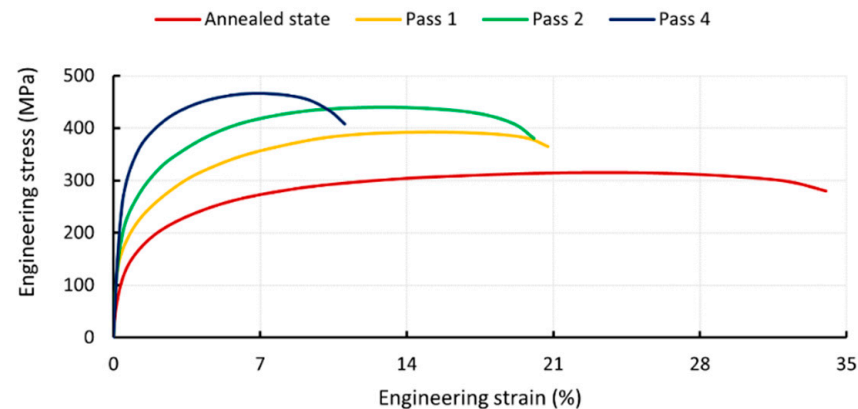


**Figure 2.** Engineering tensile stress–strain curves for the AA5052 before and after processing with the CEC method with up to four passes at room temperature, as well as the corresponding yield strength (YS), ultimate tensile strength (UTS), and elongation-to-failure (El).

**Table 1.** Mechanical properties of the AA5052, including yield strength (YS), ultimate tensile strength (UTS), and elongation-to-failure (El), before and after processing with CEC method with up to four passes at room temperature.

| Mechanical Properties | Annealed State | Pass 1 | Pass 2 | Pass 4 |
|---|---|---|---|---|
| YS (MPa) | $121.2 \pm 8$ | $177.2 \pm 6$ | $220.9 \pm 6$ | $306.8 \pm 7$ |
| UTS (MPa) | $314.5 \pm 3$ | $392.1 \pm 5$ | $439.7 \pm 6$ | $465.9 \pm 4$ |
| El (%) | $33.72 \pm 1.5$ | $20.71 \pm 2$ | $20.14 \pm 2.3$ | $11.02 \pm 1.9$ |

This improvement in mechanical strength values, including yield and ultimate tensile strength, was mainly due to considerable grain refinement (more grain boundaries, more barriers to dislocation movement, and deformation). The grain refinement occurred due to continuous accumulation of dislocations after severe plastic deformation with the CEC technique, which subsequently, through activation of restoration and recovery mechanisms, led to rearrangement of dislocations and grain refinement. It is well-documented that grain refinement, by creating barriers against dislocation movement, can improve mechanical strength [73]. This was formulated with the Hall–Petch relationship.

In many solid-solution Al alloys, such as Al-Cu, Al-Mg, and Al-Zn alloys processed with various SPD processes, a significant increase in strength and a decrease in elongation-to-failure are detectable. However, in the SPD-processed Al alloys where the second component is weakly soluble in the aluminum, such as Al-Ce and Al-La alloys [74,75], a significant

improvement in strength is accompanied by simultaneous retention of elongation-to-failure. It has also been found that elongation-to-failure is a suitable criterion for measuring the ductility of materials. In this context, ductility reduction from the application of the CEC process and addition of passes can be related to the phenomenon of strain hardening. Therefore, in order to analyze the strain-hardening behavior of AA5052 during the CEC process, the true stress-strain curves were first drawn, and then their strain-hardening exponent was derived by fitting the Holloman relationship to the uniform plastic deformation region of the curves (see Equation (3)). Based on this, the strain-hardening exponents of AA5052 before and after the first, second, and fourth passes were equal to 0.238, 0.127, 0.088, and 0.075, respectively. Therefore, roughly 47%, 63%, and 68% reductions in the value of the strain-hardening exponent were observable after applying one, two, and four passes of the CEC process as compared to the initial annealed state. This means that the strain-hardening exponent was reduced gradually with the application of the CEC process, but this reduction was intensive in the first pass. As is known, the mobility of dislocations during the CEC process is very high, which is the most significant factor in plastic deformation. On the other hand, the strain hardening exponent provides the ability to withstand the plastic deformation that prevents the dislocation motion. However, the strain hardening increases the material's strength and helps it resist the buckling effect.

$$\sigma = K\varepsilon^n \qquad (3)$$

Figure 3 represents the SEM fractography for the initial annealed state and the CEC-processed samples with different numbers of passes. As observed in the initial annealed AA5052 in Figure 3a, the grains were elongated towards the tensile axis, indicating high tensile plastic deformation failure. Some slip bands perpendicular to the fracture plane within the elongated grains also appear to indicate a necking deformation. The tensile testing results and the high elongation-to-failure also confirm this finding. In addition, a large number of deep dimples, with an average size of approximately 22 μm, indicate the sufficient ductility of the mentioned state. The presence of dimples in a fracture structure and their size, depth, and distribution is a sign of plasticity in a material. The existence of large and deep dimples indicates the perfect plasticity of an alloy, while small and shallow dimples indicate the poor plasticity of a material [76]. CEC processing (as one of the SPD techniques), by affecting the plasticity of the material, influences the size, depth, and distribution of dimples. SPD processing usually reduces the size of dimples and leads to a more homogenous distribution of dimples [77].

Regarding the CEC-processed sample after the first pass, as shown in Figure 3b, it can be stated that a ductile failure still occurred. However, the cross-sectional area of its fracture surface was slightly larger than the fracture surface of the initial material, which implies the reduction of sample ductility during the CEC process. Further, the longitudinal shear bands led to a decrease in the necking angle because of the strain-hardening effect. At the same time, dimples with an average size of 15 μm are visible. It should be noted that the number of dimples distributed homogeneously toward the internal cracks was low. The necking deformation was also visible in the second pass of the CEC-processed AA5052, as shown in Figure 3c, but the fracture cross-section and the necking angle demonstrated few changes. This indicates that there was a continuous decrease in the material's ductility in the subsequent passes, which was related to the phenomenon of strain hardening. Further, the number of observed dimples was reduced, and their average size reached 11 μm. Moreover, these heterogeneously distributed deep dimples denote severe plastic deformation during the CEC process. Eventually, in the fourth pass of the CEC-processed sample, as can be seen in Figure 3d, the shear dimples were very small due to the weak necking deformation. The fracture surface of the fourth-pass sample only demonstrated fine dimples with an average size of about 9 μm. From the above results, it can be concluded that the initial AA5052 had a suitable ductility, which means that the failure occurred in the ductile mode. However, the CEC-processed sample had a combination of ductile and brittle failure modes, and the level of the brittle failure mode increased with the addition of passes.

Investigations have shown that homogeneous ultrafine-grained (UFG) metallic materials have high strength but decreased deformation hardening capacity, which indicates lower ductility [78]. Employment of the CEC process with increases in the number of CEC passes decreased the elongation-to-failure of the samples, leading to a reduction of ductility and enhancing the tendency toward brittle failure. Usually, severe plastic deformation methods substantially decrease plasticity, which finally leads to fragility and activates the brittle mode of fracture and failure [79]. The increase the brittle failure mode in this study is also consistent with the results for the tensile properties of the AA5052 samples.
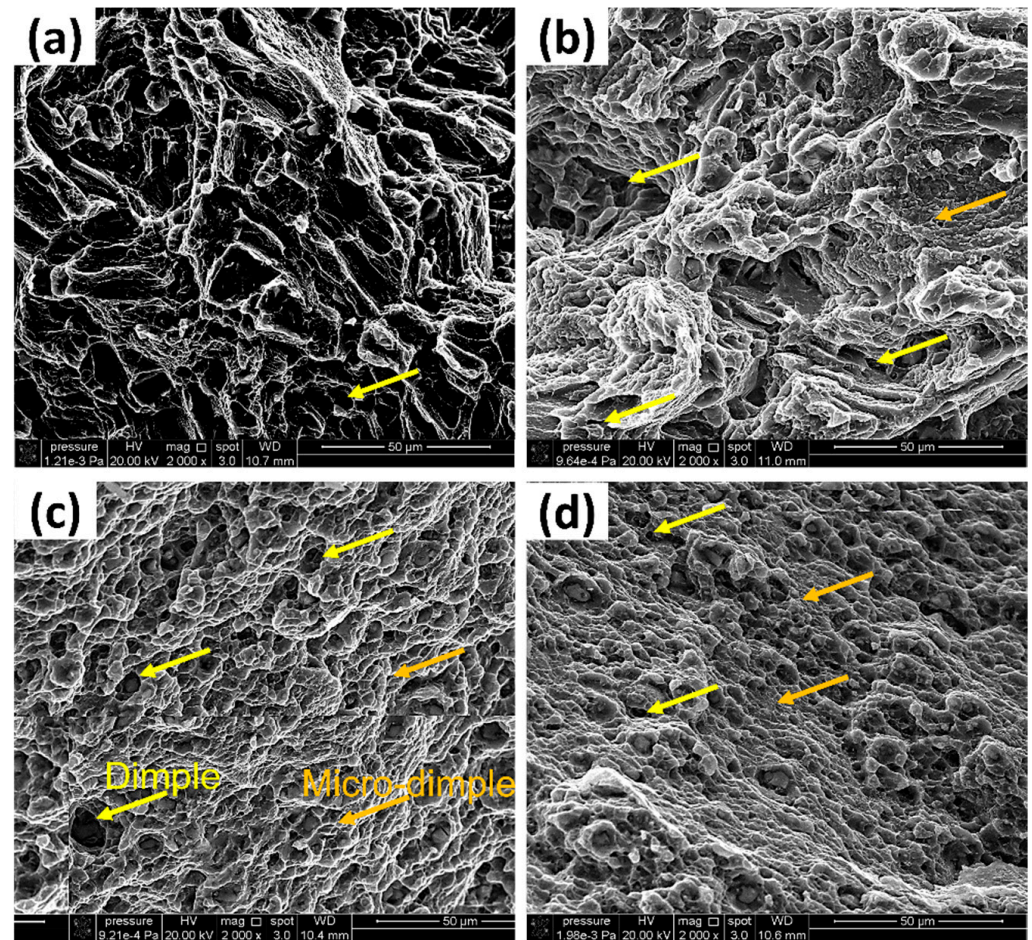


**Figure 3.** Tensile fractography morphologies of the AA5052 before and after the CEC process with different numbers of passes observed through scanning electron microscopy: (**a**) the initial annealed state, (**b**) the first pass, (**c**) the second pass, and (**d**) the fourth pass.

### 3.2. Microstructure Evolution

Figure 4 represents the OM image for the initial annealed AA5052 and the TEM images with the selected area electron diffraction (SAED) patterns for the CEC-processed samples after different numbers of passes (first, second, and fourth). As can be observed in Figure 4a, the initial state of AA5052 consisted of micro-sized grains with well-defined boundaries and an average grain size of about 23 μm. After processing aluminum samples with the CEC method, very fine and even ultrafine structures were formed in all cases, so that the grain interiors had a relatively high density of dislocations, especially in the first pass of the processed sample. In this regard, the comparison of the ring-shaped SAED pattern after the final pass sample and the dot-shaped SAED pattern after the first pass verifies that the grains were significantly refined by applying the CEC process, and this trend continued with the addition of passes.
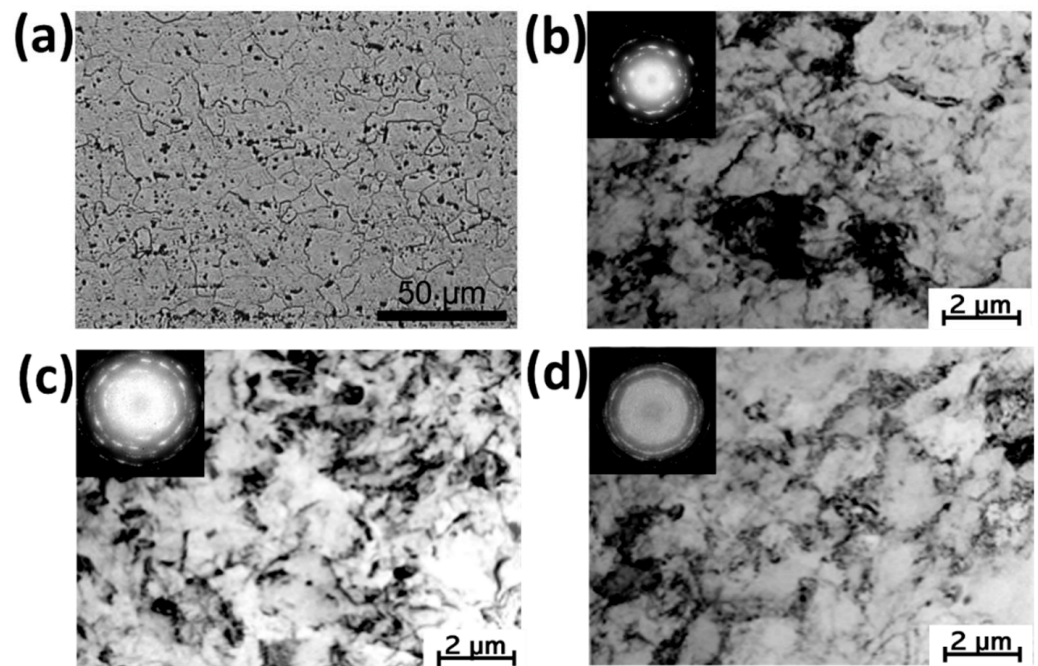
**Figure 4.** Optical microscopy and bright-field transmission electron microscopy of AA5052 (**a**) for the initial annealed state and (**b**–**d**) after processing with the CEC method with different numbers of passes: (**b**) the first pass, (**c**) the second pass, and (**d**) the fourth pass.

The microstructure of AA5052 after the first pass of the CEC method confirms that prominent structure refinement took place, such that most of the grains were highly elongated in the direction of extrusion/compression. Further, the microstructure contained numerous dislocation cells with low misorientation angles (subgrains), which were formed due to the deformation bands and oriented essentially along the deformation shear direction. A close inspection of Figure 4b,c reveals that multiple dislocations were tangled and formed grain boundaries or existed near the grain boundaries. Thus, it seems that the grain boundaries were broadened. It is also clear that the grains in the TEM image of the second pass sample were elongated further due to insufficient plastic strains. Finally, the microstructure of the final pass sample was composed of relatively equiaxial grains, most of which had well-developed grain boundaries. In this regard, the corresponding SAED pattern confirms this very fine microstructure mainly formed by high-angle grain boundaries.

It is well-established that the mobility of dislocations in grain refinement and microstructure evolution can generally be observed through the activation of dislocation-based processes, such as their dislocation glide, accumulation, interaction, tangling, and spatial rearrangement, using various models, such as the relaxed constraint, Sach zero constraint, and Taylor's full constraint. However, the most well-known and pronounced model specifically for an equiaxed structure that is consistent with the results of this study is Taylor's model, in which the simultaneous cooperation of at least five slip systems is responsible for achieving strain compatibility [80–82]. In the application of severe plastic deformation through the CEC process, continuous dislocation accumulation by increasing the number of passes leads to the formation of non-equilibrium grain boundaries, which play a significant role in the structural characterization since, during severe plastic deformation processes, the microstructure has a very high fraction of high-angle grain boundaries due to the large plastic strains, as shown in Figure 4b–d. In this regard, Figure 5 schematically illustrates the fabrication of non-equilibrium dislocation boundaries during CEC processing. This CEC-induced non-equilibrium grain boundary led to the production of excess energy and long-range elastic stresses. Further, this figure shows that the cellular structure transformed into a granular one, in which the density of dislocations in the

cell walls gradually reached a critical value. Then, dislocations with different signs were annihilated at the cell boundaries and, as a result, excess dislocations with a single sign formed at the cell boundaries. Previous studies have shown that the excess dislocations can contribute to the microstructure evolution process by playing various roles. It is clear that misorientation increases through dislocations with Burgers vectors perpendicular to the boundary and, as their density increases, they transform the microstructure into a granular one. Simultaneously, the long-range stress, along with the glide dislocations, can lead to grain segregation along the grain boundaries; i.e., rotational deformation modes. Overall, Figure 5 schematically represents the various steps in the microstructural evolution that transformed the initial coarse-grained structure (Figure 5a) into the final ultrafine-grained structure (Figure 5f). During this microstructural evolution, deformation led to the generation of numerous dislocations, which were subsequently rearranged, and the different signs of the dislocations annihilated themselves and led to the formation of dislocation walls and dislocation tangles (Figure 5c). Through further deformation, dislocations glided and climbed to form cell structures or subgrains through the activation of dynamic recovery mechanisms (Figure 5d). Dislocation motions, along with grain boundary sliding, can enhance boundary migration and subgrain rotation, which activate the nucleation process for new grains through grain boundary bulging. The grain boundary bulges are free of dislocations and are mainly generated by migration of boundaries (from the lower dislocation density side toward the higher dislocation density side). Usually, these grain boundary bulges are surrounded by accumulated dislocations, which form subgrain boundaries. Eventually, these bulges are cut apart from the original grains to produce nuclei, fabricating a "necklace structure" in the early stages of discontinuous dynamic recrystallization (DDRX; see Figure 5e). Nuclei preferentially choose high-energy, sites so they locate on or near grain boundaries and fine precipitates, which pin the movement of dislocations. In the later stages of deformation, the nuclei continue to grow through the outward migration of boundaries, consuming the newly generated dislocations through deformation until all the original grains have completely vanished, are replaced by finer recrystallized grains, and induce nanostructured or ultrafine-grained structure (see Figure 5f) [83,84].
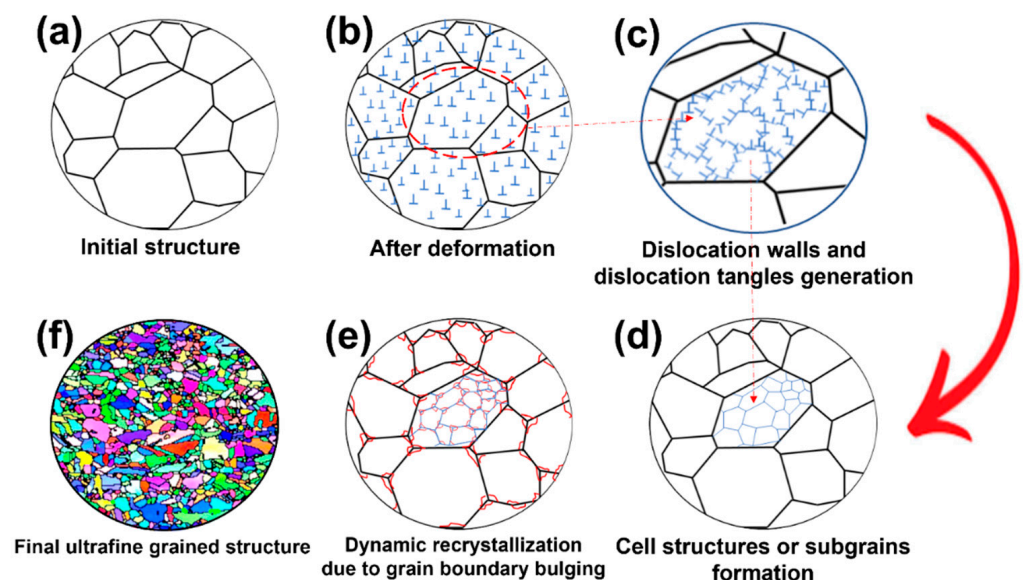


**Figure 5.** A schematical model for dislocation substructure and its evolution to final ultrafine-grained structure after CEC processing: (**a**) initial structure, (**b**) after deformation, (**c**) structure including dislocation walls and dislocation tangles, (**d**) cell structure and subgrain formation, (**e**) dynamic recrystallization and grain boundary bulging, and (**f**) an ultrafine-grained structure.

Previous studies have shown that the continuous and growing accumulation of dislocations in dislocation boundaries leads to the generation of two types of dislocation

boundary with specific characteristics and morphologies. The first type, called incidental dislocation boundaries (IDBs), is formed by trapping glide dislocations that can potentially divide the grains into cells. This type of boundary consists of a tangled dislocation structure. The second type, entitled geometrically necessary boundaries (GNBs), is generated by activating different slip systems in the grain periphery or through the subdivision of total shear strains among a set of slip planes. These GNBs can easily subdivide the grains into cell blocks and, generally, have almost planar boundaries with a regular dislocation structure. It has been found that, with a further increment of the plastic strains, the boundary spacing decreases in both IDBs and GNBs, while their misorientation angle increases. However, the alteration rate of the boundary spacing and misorientation angle is higher in GNBs than in IDBs. At high plastic strains, most dislocation boundaries, specifically GNBs, are transformed into high-angle grain boundaries due to their increased misorientation angles, resulting in the generation of an ultrafine-grained structure. The gradual transformation of dislocation boundaries at low plastic strains into high-angle boundaries at large plastic strains is known as in situ or continuous dynamic recrystallization. Hence, when this mechanism occurs and at large plastic strains, the microstructure includes a large distribution of misorientation angles with the spatial dispersion of low- and high-angle grain boundaries [83,85,86]. The microstructure of the CEC-processed AA5052 after four passes demonstrated such a situation.

$$\sigma = \sigma_0 + \sigma_{GB} + \sigma_{dis} \tag{4}$$

$$\sigma_{GB} = k/\sqrt{d_{GB}} \tag{5}$$

$$\sigma_{dis} = M\alpha Gb\sqrt{\rho_0 + \rho_{dis}} \tag{6}$$

For metals and alloys processed with different SPD processes, it is clear that the connection between the strength and structure is usually determined by the two factors of dislocation and boundary strengthening, where the contribution of the first factor is proportional to the square root of the dislocation density, while the second-factor contribution is inversely related to the square root of the boundary spacing, according to Equation (4). In this relationship, $\sigma_0$ is the friction stress, and $\sigma_{GB}$ and $\sigma_{dis}$ denote the contributions from the grain boundary strengthening and dislocation strengthening, respectively. As mentioned above, the structure is subdivided by extended lamellar boundaries nearly parallel to the extrusion plane (GNBs) and interconnecting boundaries (IDBs). Based on this, the contributions of both types of boundaries should be carefully taken into account when calculating the material strength. Therefore, the strength is based on the strengthening mechanisms, which are attributable to the different types of boundaries. In this regard, the strength contribution of the boundaries with misorientation angles greater than $15°$ is calculated with the Hall–Petch relationship, which is given in Equation (5), and the strength of the boundaries is determined based on the grain boundaries in a fully recrystallized texture-free material. In addition, the strength contribution of boundaries with misorientation angles smaller than $15°$ to the total strength, which is proportional to the square root of the dislocation density stored in the boundaries, can be obtained from Equation (6). In this regard, $k$ is the slope of the Hall–Petch relationship, $d_{GB}$ is the average spacing of boundaries that contribute to grain boundary strengthening, $M$ is the Taylor factor, $\alpha$ is a constant (0.24), $G$ is the shear modulus (26 GPa), $b$ is the Burgers vector (0.286 nm), $\rho_0$ is the dislocation density between the boundaries, and $\rho_{dis}$ is the stored dislocation density in the low-angle dislocation boundaries, which contributes as dislocation strengthening [11,87–91]. Note here that low-angle boundaries are considered cell boundaries and their strengthening is inversely proportional to the spacing of cell boundaries.

### 3.3. Wear Behavior

The wear mass loss and coefficient of friction for the AA5052 before and after the CEC process with different numbers of passes are represented in Figure 6 for two applied normal loads of 2 and 20 N. According to Figure 6a, the mass loss of the sample decreased after

applying the CEC process and adding passes. For example, at the applied normal load of 20 N, about 43.6%, 55.9%, and 71.7% reductions in the mass loss value were detectable after applying one, two, and four passes of the CEC process, respectively. This means that the wear resistance of the AA5052 improved considerably after the first pass, and the subsequent passes enhanced its value moderately. Based on this, it can be concluded that the final-pass CEC-processed sample, regardless of the amount of normal load, underwent the lowest mass loss, which was related to the effect of the material microstructural refinement. It should be noted that the mass loss can be estimated through the Archard relationship (Equation (3)). In this regard, since CEC-processed samples have higher hardness values compared to their initial annealed counterparts, as indicated in our previously published paper, it is reasonable to expect from this equation that processed samples have a lower mass loss. This theoretical finding is in good agreement with the obtained experimental results. Furthermore, based on Figure 6b, it is clear that the coefficient of friction increases for the CEC-processed samples regardless of the applied normal load. Moreover, the addition of passes increases this value. Both increments can be related to the high adhesion between the aluminum films on the used ball and the sample disc. Note that the coefficient of friction is lower when a normal load of 2 N is applied compared to the 20 N normal load. Therefore, CEC has a positive effect on the tribological behavior of AA5052, which may be attributable to the increase in the density of the grain boundaries due to the significant reduction in grain size.
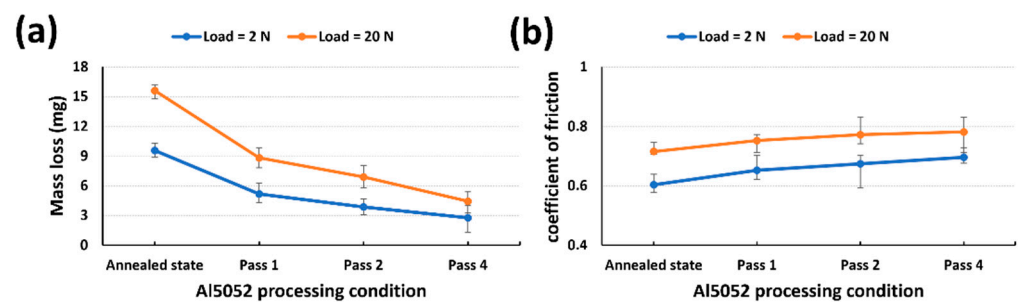


**Figure 6.** Tribological behavior of the AA5052 before and after the CEC process with different numbers of passes for two applied normal loads of 2 and 20 N: (**a**) wear mass loss and (**b**) coefficient of friction.

The worn surface morphologies of the AA5052 before and after the CEC process with different numbers of passes at the applied normal load of 2 N are shown in Figure 7. As can be seen in Figure 7a, the worn surface of the initial annealed alloy contained areas of adhesion and delamination, as well as plastic deformation bands along the sliding direction. In this regard, it seems that the material detached from the sample during the delamination process and, subsequently, adhered to the steel ball. As seen in Figure 7a, the initial sample encountered an adhesion and delamination mode of wear, which was obvious from the surface morphology. Due to the relative motion between the sample and the wearing device, the surface was sheared, resulting in the detachment of a small fragment from one surface and its attachment to another, the white particle at the bottom of Figure 7a corresponding to this case. The occurrence of the delamination mode could be confirmed by the generation of a delaminated layer that mainly arose from plastic deformation bands along the sliding direction, manifesting itself in the generation of shallow crack-like features and surface tears, as can be seen in the upper section of Figure 7a. With further sliding, the material re-adheres to the surface of the sample. By applying the CEC process and increasing the number of passes, the plastic deformation bands on the worn surface are transformed into plowing bands (the bands that form during elevated contact pressure, resulting in severe wear and the generation of deep plowing and scratching in the worn surface [92]) and the adhesion wear mechanism is attenuated. In fact, the degree of adhesive wear decreased significantly with the increase in the plastic deformation of the aluminum sample, as seen

in Figure 7b–d. The effect of adhesion wear can also be decreased by changing the surface characteristics, such as friction coefficients, hardness values, and surface energy. It is known that an increment in the surface hardness can considerably reduce adhesion wear [93], and thus the application of the CEC process with different numbers of passes can reduce the adhesion wear through an increment in the hardness. It should be noted that the wear mechanism of the worn surface of the AA5052 under the applied normal load of 20 N was the same as for the normal load of 2 N. In addition, Figure 8 shows the EDS spectrum analysis for the worn surface of the initial (Figure 8a) and CEC-processed AA5052 after four passes (Figure 8b) under an applied load of 2 N. Accordingly, the presence of Fe and O, respectively, confirm the transfer of iron from the steel ball to the aluminum sample and the formation of an oxide layer. Previous research [54,94,95] confirms the findings of this study.
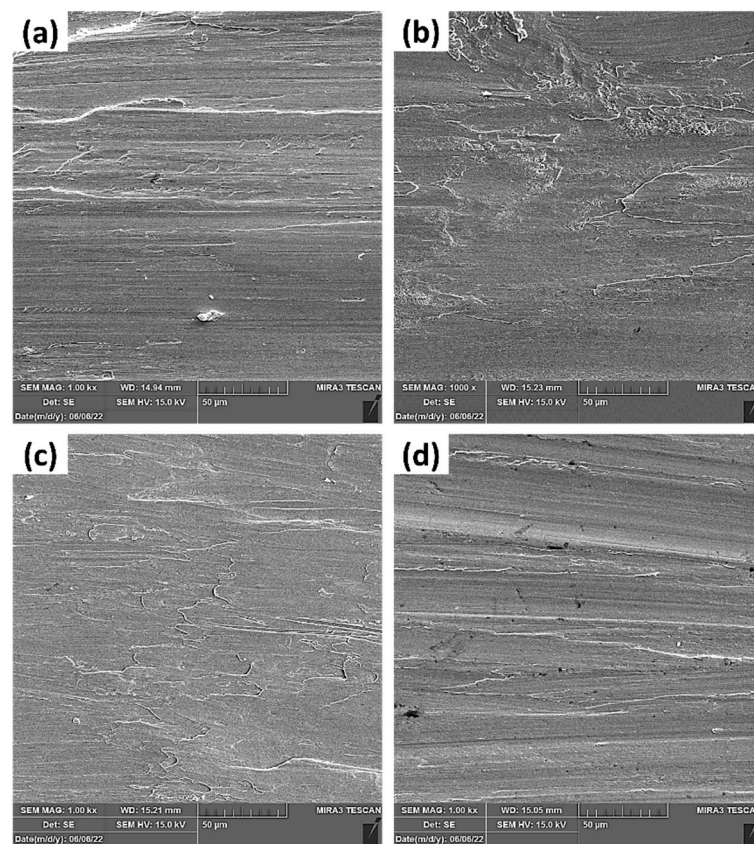


**Figure 7.** SEM images of the worn surface morphology corresponding to the AA5052 before and after the CEC process with different numbers of passes: (**a**) initial annealed state, (**b**) the first pass, (**c**) the second pass, and (**d**) the fourth pass.
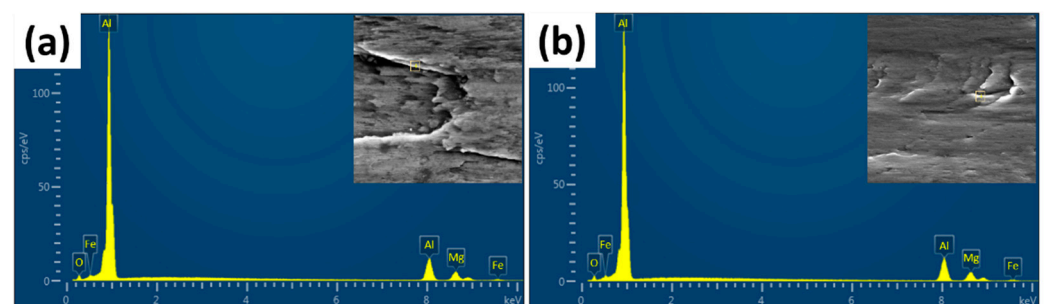


**Figure 8.** EDS analysis of the worn surface of the AA5052 tested under the applied normal load of 2 N: (**a**) initial annealed state and (**b**) after four passes with the CEC process.

## 4. Conclusions

The demand for AA5052 in different industries has increased significantly due to its reduced requirements for mass and fuel consumption and lower environmental impact. However, the problems related to AA5052 in applications that require high strength and good wear resistance have not been solved. Accordingly, this study dealt with the CEC processing of this well-known aluminum alloy at room temperature with up to four passes. Based on this, the main results can be stated as follows:

- The yield and ultimate tensile strength of the AA5052 improved significantly after the first pass, while the elongation-to-failure decreased considerably. The subsequent passes mildly changed the trend of increasing strength and reducing elongation. In this regard, the yield strength, ultimate tensile strength, and elongation-to-failure of the alloy changed from 121.2 MPa, 314.5 MPa, and 33.72% for the initial annealed state to 306.8 MPa, 465.9 MPa, and 11.02% for the final pass state, respectively. Moreover, the strain-hardening exponents of the alloy before and after the first, second, and fourth passes were 0.238, 0.127, 0.088, and 0.075, respectively;
- Grain refinement during the CEC process included the formation of dislocation cell structures, subgrain boundaries, and low-angle grain boundaries. In this regard, subgrains were developed from dislocation cells. Further, the subgrain boundaries initially became low-angle grain boundaries and, eventually, through the imposition of additional plastic strain, transformed into high-angle grain boundaries;
- The CEC process and increases in the number of passes led to a significant improvement in the wear resistance of the AA5052 due to the enhanced tensile strength from grain refinement. In this regard, the mass loss of the AA5052 in the states before and after the four-pass CEC process decreased from 15.61 mg to 4.42 mg and from 9.57 mg to 2.75 mg for the applied normal loads of 2 N and 20 N, respectively. The wear mechanism in the initial annealed alloy was a combination of adhesion and delamination with plastic deformation bands along the sliding direction. The CEC process and the increased number of passes transformed the plastic deformation bands on the worn surface into plowing ones. Further, the adhesion wear mechanism was significantly attenuated. Moreover, oxidization was found to be a mechanism contributing to wear, as oxygen was detectable under all conditions.

**Author Contributions:** Conceptualization, M.E. and S.A.; methodology, J.W.; validation, M.E., S.A. and C.G.; formal analysis, J.W. and M.E.; investigation, S.A.; resources, J.W., C.G. and M.Z.; data curation, M.E. and M.Z.; writing—original draft preparation, S.A.; writing—review and editing, M.E.; visualization, C.G. and M.Z.; supervision, M.E.; funding acquisition, M.E. All authors have read and agreed to the published version of the manuscript.

**Data Availability Statement:** All data generated or analyzed during this study are included in this published article.

## References

1. Donelan, P. Modelling microstructural and mechanical properties of ferritic ductile cast iron. *Mater. Sci. Technol.* **2000**, *16*, 261–269. [CrossRef]
2. Rosa, D.M.; Spinelli, J.E.; Osório, W.R.; Garcia, A. Effects of cell size and macrosegregation on the corrosion behavior of a dilute Pb–Sb alloy. *J. Power Sources* **2006**, *162*, 696–705. [CrossRef]
3. Petch, N.J. The Cleavage Strength of Polycrystals. *J. Iron Steel Inst.* **1953**, *174*, 25–28.
4. Bonatti, R.S.; Siqueira, R.R.; Padilha, G.S.; Bortolozo, A.D.; Osório, W.R. Distinct Alp/Sip composites affecting its densification and mechanical behavior. *J. Alloy. Compd.* **2018**, *757*, 434–447. [CrossRef]
5. Lloyd, D.J.; Court, S.A. Influence of grain size on tensile properties of Al-Mg alloys. *Mater. Sci. Technol.* **2003**, *19*, 1349–1354. [CrossRef]

6. Luo, P.; McDonald, D.; Xu, W.; Palanisamy, S.; Dargusch, M.; Xia, K. A modified Hall–Petch relationship in ultrafine-grained titanium recycled from chips by equal channel angular pressing. *Scr. Mater.* **2012**, *66*, 785–788. [CrossRef]

7. Valiev, R. Nanostructuring of metallic materials by spd processing for advanced properties. *Int. J. Mater. Res.* **2009**, *100*, 757–761. [CrossRef]

8. Valiev, R.Z.; Langdon, T.G. Principles of equal-channel angular pressing as a processing tool for grain refinement. *Prog. Mater. Sci.* **2006**, *51*, 881–981. [CrossRef]

9. Kral, P.; Dvorak, J.; Sklenicka, V.; Horita, Z.; Takizawa, Y.; Tang, Y.; Kunčická, L.; Kvapilova, M.; Ohankova, M. Influence of High Pressure Sliding and Rotary Swaging on Creep Behavior of P92 Steel at 500 °C. *Metals* **2021**, *11*, 2044. [CrossRef]

10. Langdon, T.G. Twenty-five years of ultrafine-grained materials: Achieving exceptional properties through grain refinement. *Acta Mater.* **2013**, *61*, 7035–7059. [CrossRef]

11. Ebrahimi, M.; Shaeri, M.H.; Naseri, R.; Gode, C. Equal channel angular extrusion for tube configuration of Al-Zn-Mg-Cu alloy. *Mater. Sci. Eng. A* **2018**, *731*, 569–576. [CrossRef]

12. Nazari, F.; Honarpisheh, M.; Zhao, H. The effect of microstructure parameters on the residual stresses in the ultrafine-grained sheets. *Micron* **2020**, *132*, 102843. [CrossRef] [PubMed]

13. Nazari, F.; Honarpisheh, M. Analytical and experimental investigation of deformation in constrained groove pressing process. *Proc. Inst. Mech. Eng. Part C J. Mech. Eng. Sci.* **2018**, *233*, 3751–3759. [CrossRef]

14. Zhang, Z.; Qu, S.; Feng, A.; Shen, J. Achieving grain refinement and enhanced mechanical properties in Ti–6Al–4V alloy produced by multidirectional isothermal forging. *Mater. Sci. Eng. A* **2017**, *692*, 127–138. [CrossRef]

15. Attarilar, S.; Djavanroodi, F.; Ebrahimi, M.; Al-Fadhalah, K.J.; Wang, L.; Mozafari, M. Hierarchical Microstructure Tailoring of Pure Titanium for Enhancing Cellular Response at Tissue-Implant Interface. *J. Biomed. Nanotechnol.* **2021**, *17*, 115–130. [CrossRef]

16. Fan, R.-J.; Attarilar, S.; Shamsborhan, M.; Ebrahimi, M.; Göde, C.; Özkavak, H.V. Enhancing mechanical properties and corrosion performance of AA6063 aluminum alloys through constrained groove pressing technique. *Trans. Nonferrous Met. Soc. China* **2020**, *30*, 1790–1802. [CrossRef]

17. Segal, V. Equal-Channel Angular Extrusion (ECAE): From a Laboratory Curiosity to an Industrial Technology. *Metals* **2020**, *10*, 244. [CrossRef]

18. Rogachev, S.O.; Nikulin, S.A.; Khatkevich, V.M.; Sundeev, R.V.; Komissarov, A.A. Features of Structure Formation in Layered Metallic Materials Processed by High Pressure Torsion. *Met. Mater. Trans. A* **2020**, *51*, 1781–1788. [CrossRef]

19. Ebrahimi, M.; Attarilar, S.; Djavanroodi, F.; Gode, C.; Kim, H. Wear properties of brass samples subjected to constrained groove pressing process. *Mater. Des.* **2014**, *63*, 531–537. [CrossRef]

20. Kaykha, M.M.; Dashtbayazi, M.R. An Improvement in Constrained Studded Pressing for Producing Ultra-Fine-Grained Copper Sheet. *Metals* **2022**, *12*, 193. [CrossRef]

21. Zheng, H.; Wu, R.; Hou, L.; Zhang, J.; Zhang, M. Mathematical analysis and its experimental comparisons for the accumulative roll bonding (ARB) process with different superimposed layers. *J. Magnes. Alloy.* **2021**, *9*, 1741–1752. [CrossRef]

22. Ebrahimi, M.; Shamsborhan, M. Monotonic and dynamic mechanical properties of PTCAE aluminum. *J. Alloy. Compd.* **2017**, *705*, 28–37. [CrossRef]

23. Ebrahimi, M.; Djavanroodi, F.; Tiji, S.A.N.; Gholipour, H.; Gode, C. Experimental Investigation of the Equal Channel Forward Extrusion Process. *Metals* **2015**, *5*, 471–483. [CrossRef]

24. Djavanroodi, F.; Ebrahimi, M.; Nayfeh, J.F. Tribological and mechanical investigation of multi-directional forged nickel. *Sci. Rep.* **2019**, *9*, 241. [CrossRef] [PubMed]

25. Cui, N.; Wu, Q.; Bi, K.; Wang, J.; Xu, T.; Kong, F. Effect of Multi-Directional Forging on the Microstructure and Mechanical Properties of β-Solidifying TiAl Alloy. *Materials* **2019**, *12*, 1381. [CrossRef]

26. Mahmoud, E.R.I.; Almohamadi, H.; Aljabri, A.; Khan, S.Z.; Saquib, A.N.; Farhan, M.; Elkotb, M.A.-G. Fabrication and Characterization of Steel-Base Metal Matrix Composites Reinforced by Yttria Nanoparticles through Friction Stir Processing. *Materials* **2021**, *14*, 7611. [CrossRef]

27. Ebrahimi, M.; Zhang, L.; Wang, Q.; Zhou, H.; Li, W. Damping performance of SiC nanoparticles reinforced magnesium matrix composites processed by cyclic extrusion and compression. *J. Magnes. Alloy.* **2021**, in press. [CrossRef]

28. Attarilar, S.; Salehi, M.T.; Al-Fadhalah, K.J.; Djavanroodi, F.; Mozafari, M. Functionally graded titanium implants: Characteristic enhancement induced by combined severe plastic deformation. *PLoS ONE* **2019**, *14*, e0221491. [CrossRef]

29. Shamsborhan, M.; Ebrahimi, M. Production of nanostructure copper by planar twist channel angular extrusion process. *J. Alloy. Compd.* **2016**, *682*, 552–556. [CrossRef]

30. Moazam, M.A.; Honarpisheh, M. Ring-core integral method to measurement residual stress distribution of Al-7075 alloy processed by cyclic close die forging. *Mater. Res. Express* **2019**, *6*, 0865j3. [CrossRef]

31. Richert, M. The effect of unlimited cumulation of large plastic strains on the structure-softening processes of 99.999 Al. *Mater. Sci. Eng. A* **1990**, *129*, 1–10. [CrossRef]

32. Richert, M.; Zasadziński, J.; Hawryłkiewicz, S.; Długopolski, J. Effect of large deformations on the microstructure of aluminium alloys. *Mater. Chem. Phys.* **2003**, *81*, 528–530. [CrossRef]

33. Wang, L.-P.; Jiang, W.-Y.; Chen, T.; Feng, Y.-C.; Zhou, H.-Y.; Zhao, S.-C.; Liang, Z.-Q.; Zhu, Y. Spheroidal microstructure formation and thixoforming of AM60B magnesium alloy prepared by SIMA process. *Trans. Nonferrous Met. Soc. China* **2012**, *22*, s435–s444. [CrossRef]

34. Peng, T.; Wang, Q.; Han, Y.; Zheng, J.; Guo, W. Consolidation behavior of Mg–10Gd–2Y–0.5Zr chips during solid-state recycling. *J. Alloy. Compd.* **2010**, *503*, 253–259. [CrossRef]

35. Chen, Y.-J.; Wang, Q.-D.; Lin, J.-B.; Liu, M.-P.; Hjelen, J.; Roven, H.J. Grain refinement of magnesium alloys processed by severe plastic deformation. *Trans. Nonferrous Met. Soc. China* **2014**, *24*, 3747–3754. [CrossRef]

36. Torabi, H.; Faraji, G.; Masoumi, A. Processing characterization of binary Mg-Zn alloys fabricated by a new powder consolidation combined severe plastic deformation method. *J. Alloy. Compd.* **2020**, *832*, 154922. [CrossRef]

37. Ebrahimi, M.; Wang, Q.; Attarilar, S. A comprehensive review of magnesium-based alloys and composites processed by cyclic extrusion compression and the related techniques. *Prog. Mater. Sci.* **2023**, *131*, 101016. [CrossRef]

38. Starke, E.A., Jr.; Staley, J.T. Application of modern aluminum alloys to aircraft. *Prog. Aerosp. Sci.* **1996**, *32*, 131–172. [CrossRef]

39. Wan, B.; Chen, W.; Lu, T.; Liu, F.; Jiang, Z.; Mao, M. Review of solid state recycling of aluminum chips. *Resour. Conserv. Recycl.* **2017**, *125*, 37–47. [CrossRef]

40. Ebrahimi, M.; Gholipour, H.; Djavanroodi, F. A study on the capability of equal channel forward extrusion process. *Mater. Sci. Eng. A* **2016**, *650*, 1–7. [CrossRef]

41. Attarilar, S.; Ebrahimi, M.; Hsieh, T.-H.; Uan, J.-Y.; Göde, C. An insight into the vibration-assisted rolling of AA5052 aluminum alloy: Tensile strength, deformation microstructure, and texture evolution. *Mater. Sci. Eng. A* **2021**, *803*, 140489. [CrossRef]

42. Ebrahimi, M.; Liu, G.; Wang, Q.; Jiang, H.; Ding, W.; Shang, Z.; Luo, L. Evaluation of interface structure and high-temperature tensile behavior in Cu/Al8011/Al5052 trilayered composite. *Mater. Sci. Eng. A* **2020**, *798*, 140129. [CrossRef]

43. Ansarian, I.; Shaeri, M.; Ebrahimi, M.; Minárik, P.; Bartha, K. Microstructure evolution and mechanical behaviour of severely deformed pure titanium through multi directional forging. *J. Alloy. Compd.* **2019**, *776*, 83–95. [CrossRef]

44. Bhardwaj, A.; Gupta, A.K.; Padisala, S.K.; Poluri, K. Characterization of mechanical and microstructural properties of constrained groove pressed nitinol shape memory alloy for biomedical applications. *Mater. Sci. Eng. C* **2019**, *102*, 730–742. [CrossRef]

45. Miura, H.; Yu, G.; Yang, X. Multi-directional forging of AZ61Mg alloy under decreasing temperature conditions and improvement of its mechanical properties. *Mater. Sci. Eng. A* **2011**, *528*, 6981–6992. [CrossRef]

46. Murashkin, M.Y.; Sabirov, I.; Sauvage, X.; Valiev, R.Z. Nanostructured Al and Cu alloys with superior strength and electrical conductivity. *J. Mater. Sci.* **2016**, *51*, 33–49. [CrossRef]

47. Moazam, M.; Honarpisheh, M. The effects of combined cyclic close die forging and aging process on microstructure and mechanical properties of AA7075. *Proc. Inst. Mech. Eng. Part L J. Mater. Des. Appl.* **2020**, *234*, 1242–1251. [CrossRef]

48. Wu, J.; Djavanroodi, F.; Shamsborhan, M.; Attarilar, S.; Ebrahimi, M. Improving Mechanical and Corrosion Behavior of 5052 Aluminum Alloy Processed by Cyclic Extrusion Compression. *Metals* **2022**, *12*, 1288. [CrossRef]

49. Takata, N.; Lee, S.-H.; Tsuji, N. Ultrafine grained copper alloy sheets having both high strength and high electric conductivity. *Mater. Lett.* **2009**, *63*, 1757–1760. [CrossRef]

50. Ebrahimi, M.; Zhang, L.; Wang, Q.; Zhou, H.; Li, W. Damping characterization and its underlying mechanisms in CNTs/AZ91D composite processed by cyclic extrusion and compression. *Mater. Sci. Eng. A* **2021**, *821*, 141605. [CrossRef]

51. Révész, Á.; Gajdics, M.; Varga, L.K.; Krállics, G.; Péter, L.; Spassov, T. Hydrogen storage of nanocrystalline Mg–Ni alloy processed by equal-channel angular pressing and cold rolling. *Int. J. Hydrog. Energy* **2014**, *39*, 9911–9917. [CrossRef]

52. Moazam, M.; Honarpisheh, M. Improving the mechanical properties and reducing the residual stresses of AA7075 by combination of cyclic close die forging and precipitation hardening. *Proc. Inst. Mech. Eng. Part L J. Mater. Des. Appl.* **2021**, *235*, 542–549. [CrossRef]

53. Ramanathan, T.; Sekar, K.; Shanmugam, N. Microstructural Evaluation and Effect of Heat Generation in FSW of AA1100. *Chiang Mai J. Sci.* **2022**, *49*, 487–495. [CrossRef]

54. El Aal, M.I.A.; El Mahallawy, N.; Shehata, F.A.; El Hameed, M.A.; Yoon, E.Y.; Kim, H.S. Wear properties of ECAP-processed ultrafine grained Al–Cu alloys. *Mater. Sci. Eng. A* **2010**, *527*, 3726–3732. [CrossRef]

55. Gao, L.; Cheng, X. Microstructure and dry sliding wear behavior of Cu–10%Al–4%Fe alloy produced by equal channel angular extrusion. *Wear* **2008**, *265*, 986–991. [CrossRef]

56. Gao, L.; Cheng, X. Microstructure, phase transformation and wear behavior of Cu–10%Al–4%Fe alloy processed by ECAE. *Mater. Sci. Eng. A* **2008**, *473*, 259–265. [CrossRef]

57. Korshunov, L.G.; Noskova, N.I.; Korznikov, A.V.; Chernenko, N.L.; Vil'Danova, N.F. Effect of severe plastic deformation on the microstructure and tribological properties of a babbit B83. *Phys. Met. Met.* **2009**, *108*, 519–526. [CrossRef]

58. Wang, Z.; Tao, N.; Li, S.; Wang, W.; Liu, G.; Lu, J.; Lu, K. Effect of surface nanocrystallization on friction and wear properties in low carbon steel. *Mater. Sci. Eng. A* **2003**, *352*, 144–149. [CrossRef]

59. La, P.; Ma, J.; Zhu, Y.T.; Yang, J.; Liu, W.; Xue, Q.; Valiev, R.Z. Dry-sliding tribological properties of ultrafine-grained Ti prepared by severe plastic deformation. *Acta Mater.* **2005**, *53*, 5167–5173. [CrossRef]

60. Kucukomeroglu, T. Effect of equal-channel angular extrusion on mechanical and wear properties of eutectic Al–12Si alloy. *Mater. Des.* **2010**, *31*, 782–789. [CrossRef]

61. Kim, Y.-S.; Yu, H.S.; Shin, D.H. Low sliding-wear resistance of ultrafine-grained Al alloys and steel having undergone severe plastic deformation. *Int. J. Mater. Res.* **2009**, *100*, 871–874. [CrossRef]

62. Kim, Y.S.; Ha, J.; Kim, W.J. Dry Sliding Wear Characteristics of Severely Deformed 6061 Aluminum and AZ61 Magnesium Alloys. *Mater. Sci. Forum* **2004**, *449–452*, 597–600. [CrossRef]

63. Sato, H.; El Hadad, S.; Sitdikov, O.; Watanabe, Y. Effects of Processing Routes on Wear Property of Al-Al3Ti Alloys Severely Deformed by ECAP. *Mater. Sci. Forum* **2008**, *584–586*, 971–976. [CrossRef]
64. Garbacz, H.; Grądzka-Dahlke, M.; Kurzydłowski, K.J. The tribological properties of nano-titanium obtained by hydrostatic extrusion. *Wear* **2007**, *263*, 572–578. [CrossRef]
65. Sułkowski, B.; Janoska, M.; Boczkal, G.; Chulist, R.; Mroczkowski, M.; Pałka, P. The effect of severe plastic deformation on the Mg properties after CEC deformation. *J. Magnes. Alloy.* **2020**, *8*, 761–768. [CrossRef]
66. El-Garhy, G.; El Mahallawy, N.; Shoukry, M. Effect of grain refining by cyclic extrusion compression (CEC) of Al-6061 and Al-6061/SiC on wear behavior. *J. Mater. Res. Technol.* **2021**, *12*, 1886–1897. [CrossRef]
67. Ansarian, I.; Shaeri, M.H.; Ebrahimi, M.; Minárik, P. Tribological Characterization of Commercial Pure Titanium Processed by Multi-Directional Forging. *Acta Met. Sin. (Engl. Lett.)* **2019**, *32*, 857–868. [CrossRef]
68. Shaeri, M.; Ebrahimi, M.; Salehi, M.; Seyyedein, S.H. Effect of ECAP temperature on microstructure and mechanical properties of Al–Zn–Mg–Cu alloy. *Prog. Nat. Sci.* **2016**, *26*, 182–191. [CrossRef]
69. Sabbaghianrad, S.; Langdon, T.G. A critical evaluation of the processing of an aluminum 7075 alloy using a combination of ECAP and HPT. *Mater. Sci. Eng. A* **2014**, *596*, 52–58. [CrossRef]
70. Djavanroodi, F.; Ebrahimi, M.; Rajabifar, B.; Akramizadeh, S. Fatigue design factors for ECAPed materials. *Mater. Sci. Eng. A* **2010**, *528*, 745–750. [CrossRef]
71. Kawasaki, M.; Foissey, J.; Langdon, T.G. Development of hardness homogeneity and superplastic behavior in an aluminum–copper eutectic alloy processed by high-pressure torsion. *Mater. Sci. Eng. A* **2013**, *561*, 118–125. [CrossRef]
72. Yogesha, K.K.; Kumar, N.; Joshi, A.; Jayaganthan, R.; Nath, S.K. A Comparative Study on Tensile and Fracture Behavior of Al–Mg Alloy Processed Through Cryorolling and Cryo Groove Rolling. *Met. Microstruct. Anal.* **2016**, *5*, 251–263. [CrossRef]
73. Li, C.; Mei, Q.; Li, J.; Chen, F.; Ma, Y.; Mei, X. Hall-Petch relations and strengthening of Al-ZnO composites in view of grain size relative to interparticle spacing. *Scr. Mater.* **2018**, *153*, 27–30. [CrossRef]
74. Medvedev, A.E.; Murashkin, M.Y.; Enikeev, N.A.; Bikmukhametov, I.; Valiev, R.Z.; Hodgson, P.D.; Lapovok, R. Effect of the eutectic Al-(Ce,La) phase morphology on microstructure, mechanical properties, electrical conductivity and heat resistance of Al-4.5(Ce,La) alloy after SPD and subsequent annealing. *J. Alloy. Compd.* **2019**, *796*, 321–330. [CrossRef]
75. Rogachev, S.O.; Naumova, E.A.; Lukina, E.A.; Zavodov, A.V.; Khatkevich, V.M. High Strength Al–La, Al–Ce, and Al–Ni Eutectic Aluminum Alloys Obtained by High-Pressure Torsion. *Materials* **2021**, *14*, 6404. [CrossRef]
76. Sun, Y.; Chang, H.; Fang, Z.; Dong, Y.; Dan, Z.; Guo, Y.; Zhou, L. Study on Microstructure and Mechanical Properties of Low Cost Ti-Fe-B Alloy. *MATEC Web Conf.* **2020**, *321*, 11029. [CrossRef]
77. El Aal, M.I.A. The influence of ECAP and HPT processing on the microstructure evolution, mechanical properties and tribology characteristics of an Al6061 alloy. *J. Mater. Res. Technol.* **2020**, *9*, 12525–12546. [CrossRef]
78. Valiev, R.Z.; Alexandrov, I.V.; Zhu, Y.T.; Lowe, T.C. Paradox of Strength and Ductility in Metals Processed Bysevere Plastic Deformation. *J. Mater. Res.* **2002**, *17*, 5–8. [CrossRef]
79. Valiev, R.Z.; Estrin, Y.; Horita, Z.; Langdon, T.G.; Zehetbauer, M.J.; Zhu, Y. Producing Bulk Ultrafine-Grained Materials by Severe Plastic Deformation: Ten Years Later. *JOM* **2016**, *68*, 1216–1226. [CrossRef]
80. Moradpour, M.; Khodabakhshi, F.; Eskandari, H. Dynamic strain aging behavior of an ultra-fine grained Al-Mg alloy (AA5052) processed via classical constrained groove pressing. *J. Mater. Res. Technol.* **2019**, *8*, 630–643. [CrossRef]
81. Liu, M.; Roven, H.J.; Yu, Y.; Werenskiold, J.C. Deformation structures in 6082 aluminium alloy after severe plastic deformation by equal-channel angular pressing. *Mater. Sci. Eng. A* **2008**, *483-484*, 59–63. [CrossRef]
82. Kamikawa, N.; Huang, X.; Tsuji, N.; Hansen, N. Strengthening mechanisms in nanostructured high-purity aluminium deformed to high strain and annealed. *Acta Mater.* **2009**, *57*, 4198–4208. [CrossRef]
83. Sakai, T.; Belyakov, A.; Kaibyshev, R.; Miura, H.; Jonas, J.J. Dynamic and post-dynamic recrystallization under hot, cold and severe plastic deformation conditions. *Prog. Mater. Sci.* **2014**, *60*, 130–207. [CrossRef]
84. Humphreys, F.J.; Hatherly, M. The Mobility and Migration of Boundaries. In *Recrystallization and Related Annealing Phenomena*; Elsevier: Amsterdam, The Netherlands, 2004; pp. 121–167.
85. Kaibyshev, R.; Malopheyev, S. Mechanisms of Dynamic Recrystallization in Aluminum Alloys. *Mater. Sci. Forum* **2014**, *794–796*, 784–789. [CrossRef]
86. Gourdet, S.; Montheillet, F. A model of continuous dynamic recrystallization. *Acta Mater.* **2003**, *51*, 2685–2699. [CrossRef]
87. Zhilyaev, A.; Shakhova, I.; Morozova, A.; Belyakov, A.; Kaibyshev, R. Grain refinement kinetics and strengthening mechanisms in Cu–0.3Cr–0.5Zr alloy subjected to intense plastic deformation. *Mater. Sci. Eng. A* **2015**, *654*, 131–142. [CrossRef]
88. Cabibbo, M. Microstructure strengthening mechanisms in different equal channel angular pressed aluminum alloys. *Mater. Sci. Eng. A* **2013**, *560*, 413–432. [CrossRef]
89. Lanjewar, H.; Kestens, L.A.; Verleysen, P. Damage and strengthening mechanisms in severely deformed commercially pure aluminum: Experiments and modeling. *Mater. Sci. Eng. A* **2021**, *800*, 140224. [CrossRef]
90. Morris, D.G.; Gutierrez-Urrutia, I.; Muñoz-Morris, M.A. Analysis of strengthening mechanisms in a severely-plastically-deformed Al–Mg–Si alloy with submicron grain size. *J. Mater. Sci.* **2007**, *42*, 1439–1443. [CrossRef]
91. Morris, D. Strengthening mechanisms in nanocrystalline metals. In *Nanostructured Metals and Alloys*; Elsevier: Amsterdam, The Netherlands, 2011; pp. 299–328.

92.　Zhang, P.; Zhang, F.; Yan, Z.; Wang, T.; Qian, L. Wear property of low-temperature bainite in the surface layer of a carburized low carbon steel. *Wear* **2011**, *271*, 697–704. [CrossRef]

93.　Lü, W.; Li, G.; Zhou, Y.; Liu, S.; Wang, K.; Wang, Q. Effect of high hardness and adhesion of gradient TiAlSiN coating on cutting performance of titanium alloy. *J. Alloy. Compd.* **2020**, *820*, 153137. [CrossRef]

94.　Ortiz-Cuellar, E.; Hernandez-Rodriguez, M.A.L.; Sanchez, E.G. Evaluation of the tribological properties of an Al–Mg–Si alloy processed by severe plastic deformation. *Wear* **2011**, *271*, 1828–1832. [CrossRef]

95.　Wang, C.T.; Gao, N.; Wood, R.; Langdon, T.G. Wear behavior of an aluminum alloy processed by equal-channel angular pressing. *J. Mater. Sci.* **2011**, *46*, 123–130. [CrossRef]